JACS
JOURNAL OF THE AMERICAN CHEMICAL SOCIETY

ARTICLE

pubs.acs.org/JACS

Theoretical Evaluation of Structural Models of the S_2 State in the Oxygen Evolving Complex of Photosystem II: Protonation States and Magnetic Interactions

William Ames,[†] Dimitrios A. Pantazis,[†] Vera Krewald,[†] Nicholas Cox,[†] Johannes Messinger,[*,‡] Wolfgang Lubitz,[*,†] and Frank Neese[*,†]

[†]Max-Planck-Institut für Bioanorganische Chemie, Stiftstr. 34-36, D-45470 Mülheim an der Ruhr, Germany

[‡]Institutionen för Kemi, Kemiskt Biologiskt Centrum, Umeå Universitet, Linnaeus väg 6, S-90187 Umeå, Sweden

Supporting Information Web-Enhanced

ABSTRACT: Protonation states of water ligands and oxo bridges are intimately involved in tuning the electronic structures and oxidation potentials of the oxygen evolving complex (OEC) in Photosystem II, steering the mechanistic pathway, which involves at least five redox state intermediates S_n (n = 0−4) resulting in the oxidation of water to molecular oxygen. Although protons are practically invisible in protein crystallography, their effects on the electronic structure and magnetic properties of metal active sites can be probed using spectroscopy. With the twin purpose of aiding the interpretation of the complex electron paramagnetic resonance (EPR) spectroscopic data of the OEC and of improving the view of the cluster at the atomic level, a complete set of protonation configurations for the S_2 state of the OEC were investigated, and their distinctive effects on magnetic properties of the cluster were evaluated. The most recent X-ray structure of Photosystem II at 1.9 Å resolution was used and refined to obtain the optimum structure for the Mn_4O_5Ca core within the protein pocket. Employing this model, a set of 26 structures was constructed that tested various protonation scenarios of the water ligands and oxo bridges. Our results suggest that one of the two water molecules that are proposed to coordinate the outer Mn ion (Mn_A) of the cluster is deprotonated in the S_2 state, as this leads to optimal experimental agreement, reproducing the correct ground state spin multiplicity (S = 1/2), spin expectation values, and EXAFS-derived metal−metal distances. Deprotonation of Ca^{2+}-bound water molecules is strongly disfavored in the S_2 state, but dissociation of one of the two water ligands appears to be facile. The computed isotropic hyperfine couplings presented here allow distinctions between models to be made and call into question the assumption that the largest coupling is always attributable to Mn^{III}. The present results impose limits for the total charge and the proton configuration of the OEC in the S_2 state, with implications for the cascade of events in the Kok cycle and for the water splitting mechanism.

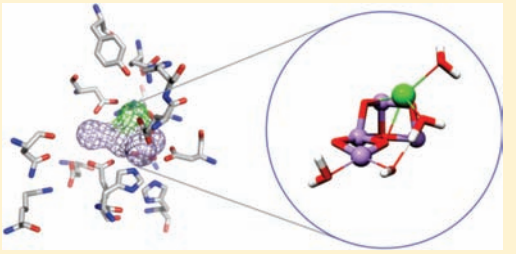

1. INTRODUCTION

The promise of safe, secure, and sustainable solar energy conversion is driving research into natural and artificial photosynthesis across a wide spectrum of scientific disciplines.[1−4] A major endeavor in this field is directed at gaining detailed, atomic-level information about the structure, physical properties, and mechanistic function of the components of the natural photosynthetic apparatus. Oxygenic photosynthesis accomplishes the conversion of water and carbon dioxide to carbohydrates and molecular oxygen. This deceptively simple reaction requires one of the most complicated biochemical mechanisms evolved on Earth.[5]

The initial steps of photosynthesis take place in Photosystem II (PSII), a multisubunit protein complex embedded in the thylakoid membranes of green plants, algae, and cyanobacteria. PSII employs the energy of sunlight to extract electrons from water to reduce an exchangeable plastoquinone (Q_B). Light excitation produces a charge-separated state in the PSII reaction center (P680), which is stabilized by a cascade of electron transfer steps across the lipid bilayer. In rapid succession, the electron is passed to Q_B on the stromal surface of the PSII complex. Following two sequential reductions, the doubly protonated Q_BH_2 leaves PSII, allowing these electrons to be passed to the next element of the photosynthetic electron transfer chain: the cytochrome b_6f complex, which in turn passes electrons to photosystem I (PSI) via the mobile electron carrier plastocyanin. Ultimately, water-derived electrons are used in the Calvin−Benson cycle to reduce CO_2 to carbohydrates. $P680^{\bullet+}$ is reduced by a redox-active tyrosine residue (Y_Z), which in turn is reduced by the oxygen evolving complex (OEC)—also called the water oxidizing complex (WOC), the catalytic site where two molecules of water are transformed into dioxygen, four protons, and four electrons.

The OEC is an oxo-bridged cluster of four manganese and one calcium ions (Mn_4O_5Ca), embedded in a functionally important protein matrix. Its operation depends on its ability to accumulate four oxidizing equivalents by cycling through five oxidation

Received: May 14, 2011
Published: November 17, 2011

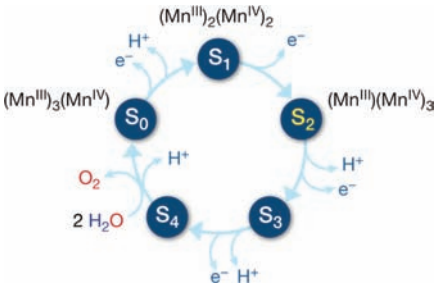

Figure 1. The Kok cycle, indicating the sequence of proton and electron transfer events at each S-state transition, along with the most probable oxidation states of the cluster. Probable oxidation states for the S_3 and S_4 states of the Kok cycle are currently being debated and have not been indicated here.

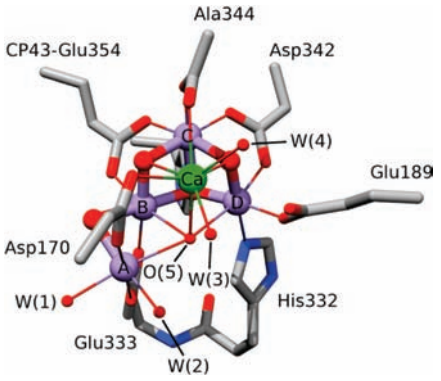

Figure 2. The structure of the OEC and its immediate environment as determined by Umena et al. at 1.9 Å resolution.[19] Manganese, calcium, carbon, nitrogen, and oxygen atoms are shown in purple, green, gray, blue, and red, respectively.

states, known as the S_0-S_4 states of the Kok cycle (Figure 1).[6,7] For each step of the cycle, an electron is transferred from the cluster to the nearby Y_Z (D1-Tyr161). When the cluster reaches the as yet unobserved, highly reactive S_4 state(s), O_2 is released, and the system decays back to S_0. Water oxidation relies on a delicately orchestrated sequence of proton and electron transfer steps, in which the release of protons is essential to maintain a redox potential low enough for the next oxidation event to occur. According to our current understanding of the Kok cycle, proton transfer from the OEC into the lumen occurs with a 1:0:1:2 periodicity,[8] within a strictly alternate sequence of electron and proton transfer steps.[9,10] The only oxidation step that is not accompanied by a concomitant proton transfer is the $S_1 \rightarrow S_2$ transition, which is also known to involve minimal structural reorganization of the inorganic cluster.[11]

In the years following the publication of the first crystal structure of PSII,[12] the persistent efforts of several different research groups have yielded a number of structures of progressively higher resolution, constantly improving our understanding of PSII.[13−19] To date, a solid understanding of the arrangement and organization of various cofactors for PSII has been achieved, including the position of the chloride ion(s),[18−21] an important additional cofactor for water splitting, with distances of 6.7−7.4 Å from the OEC core and distances of greater than 9 Å from the Ca^{2+} cofactor. For years, the low resolution in the region of the water oxidation active site and the radiation damage resulting from photoreduction of the manganese ion prohibited the attainment of an atomistic view of the cluster.[23] However, Umena et al. very recently reported a structure of PSII at a significantly improved resolution of 1.9 Å (Figure 2).[19] This jump of 1 Å in resolution compared to the best previous structure of PSII (2.9 Å)[17] allows the assignment of the protein residues around the cluster and the coordination modes of the ligating amino acids with high certainty. Most importantly, the metal ions of the OEC are clearly visible for the first time; the positions of the oxo bridges can be deduced with some confidence; and four "water" molecules (of unknown protonation states) are shown to be ligands to the cluster, two of them coordinated to Mn_A and the other two to calcium.

As will be shown in the following, when it comes to the connectivity of the OEC core, the proposed crystallographic model cannot be considered exact. In particular, the precise positions of the oxo bridges and the bonding within the manganese cluster need to be refined to achieve agreement with other experimentally known properties of the OEC. Besides, the protonation pattern of the OEC in each state of the Kok cycle—a critical determinant of electronic structure and mechanism—must also be derived by methods other than crystallography. The role of spectroscopy is crucial in this respect. Extended X-ray absorption fine structure (EXAFS) and polarized EXAFS have yielded accurate information about the number, length, and orientation of Mn···Mn and Mn···Ca vectors, providing reliable measures for the validation of plausible theoretical or crystallographic structural models of the OEC.[11,24−28] Specifically, EXAFS studies have firmly established the presence of three short (2.7−2.8 Å in a 2:1 ratio) and one longer (3.2 Å) Mn···Mn distances in the S_1 state of the cluster,[26] while four Mn···Ca(Sr) distances and their S-state dependence have also been derived (short, ∼3.5 Å, and long, ∼4.0 Å, in a 3:1 or 2:2 ratio).[11] X-ray absorption and emission spectroscopy (XAS, XES), as well as resonant inelastic X-ray scattering spectroscopy (RIXS), have been used to probe the Mn oxidation states of the cluster during S-state advancement.[29−32] Electron paramagnetic resonance (EPR) and electron−nuclear double resonance (ENDOR) techniques offer invaluable insight into the electronic structure of the OEC, in terms of the coupling between the Mn ions, as well as oxidation and spin states.[33−41] The selectivity and sensitivity of EPR has been particularly important in characterizing the S_2 state of the OEC, which exhibits a multiline signal attributed to a spin 1/2 ground state.[42,43] The hyperfine coupling constants of ^{55}Mn provide information about the electronic structure of the S_2 state and form a solid reference against which hypothetical structural models can be validated.

Input from theoretical studies can be of great value in understanding experimental observations and relating spectral features to particular structural details, especially in the case of the OEC where the complexity of spectroscopic data often prevents interpretation in terms of a unique model. Quantum chemistry offers a unifying framework for the convergence of different research approaches and for the simultaneous evaluation of data sourced from diverse physicochemical methods. Indeed, theoretical investigations have made a significant contribution to photosynthesis research,[44−47] whether they focus on structure, mechanism, magnetism, or spectroscopy.[47−67] The research program pursued in our group focuses on development and application of methods for predicting spectroscopic properties of potential OEC models and emphasizes comparison with the abundant experimental data obtained over the years through EPR and related techniques. Cross-validation against experimentally determined spectroscopic parameters is especially

important if several energetically similar structures exist for the complex of interest.

With this guiding principle and well-calibrated methods in hand,[66,68] in the present paper we first refine the 1.9 Å crystallographic structure of the OEC to arrive at a model for the S_2 state of the OEC that features optimal chemical bonding and is consistent with EXAFS data. This model is then used to probe the protonation states of the OEC and to determine how specific protonation patterns may map onto spectroscopic properties. The different protonation patterns of the Mn-ligated water molecules (including substrate waters) and the oxo bridges that bind the Mn ions and mediate the electronic and magnetic interactions between them are expected to define the electronic structure of the cluster and hence its magnetic and spectroscopic properties. The goal is to examine how different protonation states of ligated water molecules and oxo bridges affect the magnetic coupling in the S_2 state of the OEC and therefore the total spin state of the cluster, the individual site-spin expectation values for each ion, and the spectroscopic properties such as the hyperfine couplings, which can be probed by EPR techniques. It is shown that different protonation patterns lead to clearly discernible spin projections and ^{55}Mn hyperfine coupling parameters. By distinguishing between protonation patterns that agree with experiment and those that do not, it becomes possible to limit the multitude of conceivable states to a small number of spectroscopically consistent isomers. Besides determining the spectroscopic signatures of protonation states, the results obtained in this paper propose limits for the total charge of the OEC site at a given state and therefore provide additional insight into the sequential steps of proton and electron transfers. The mechanistic implications of these findings for the Kok cycle are discussed.

2. COMPUTATIONAL METHODS

2.1. Geometry Optimizations. Geometries of all models were optimized in their high-spin states.[66−72] The oxidation states of the Mn ions in the S_2 state are assigned as $Mn_3^{IV}Mn^{III}$. Oxidation states for each Mn ion were determined by examination of the Mulliken spin populations, such that Mn^{IV} and Mn^{III} have calculated spin populations of approximately 2.8 and 3.9, respectively.[68] All structures were optimized with the BP86 density functional,[73,74] which is known to yield more realistic bond lengths for first-row transition metal systems than hybrid functionals.[45,75−77] Given the deficiencies of DFT in treating dispersion interactions in general[78−80] and their effect on transition metal systems in particular,[81] the optimizations included the third-generation (D3) semiempirical van der Waals corrections proposed by Grimme.[82] Relativistic corrections were found to be non-negligible for geometries and energies, thus all calculations were performed using the zeroth-order regular approximation (ZORA) Hamiltonian to include scalar relativistic effects.[83−85] ZORA-adapted segmented all-electron relativistically contracted (SARC) basis sets were employed for all atoms.[86] ZORA-recontracted versions of the def2-SVP basis sets were used for C and H atoms, while ZORA versions of def2-TZVP basis sets were used for all other atoms, removing f functions for main-group elements.[86,87] Use of triple-ζ polarized basis sets for the atoms comprising the Mn_4O_5Ca core was found to be critical in obtaining converged geometric parameters. The conductor-like screening model (COSMO)[88,89] with a dielectric constant of $\varepsilon = 8.0$ was used to ensure that optimized geometries reflect the approximate effects of the protein environment. Optimizations were carried out both with and without backbone constraints; fully relaxed structures were used in evaluations of spectroscopic parameters. The calculations employed the RI approximation with decontracted auxiliary def2-TZVP/J Coulomb fitting basis sets.[90,91] Increased integration grids ("Grid4" in ORCA convention) and tight SCF convergence criteria were used throughout.

2.2. Exchange Couplings and Spin States. Calculations of exchange coupling constants were performed using the broken-symmetry DFT methodology (BS-DFT).[76,92−94] The magnetic interactions between the manganese centers are assumed to follow the isotropic Heisenberg−Dirac−van Vleck (HDvV) Hamiltonian of eq 1

$$H_{\mathrm{HDvV}} = -2\sum_{i<j} J_{ij}\hat{S}_i\hat{S}_j \tag{1}$$

There are six possible exchange couplings J_{ij} in a system of four magnetic ions. To ensure generality, the exact problem is solved without any assumptions about the magnitude of non-nearest neighbor interactions. A system of four centers with fixed local spins has one high-spin single-determinant representation (total $M_S = 13/2$ in the present case) and seven BS single-determinant representations arising from all mutually parallel/antiparallel (±) combinations of the four local M_S values. In the present case of three Mn^{IV} and one Mn^{III} centers with fixed atomic high-spin d^3 or d^4 electronic configurations, there are three BS solutions with total M_S of 7/2, one with total $M_S = 5/2$, and three with total $M_S = 1/2$. The energies of the BS solutions have little meaning taken in isolation but serve to extract the exchange coupling constants that are transferable to the HDvV Hamiltonian. Although eight computed energies can be obtained with BS-DFT, the energy spectrum described by the coupling of the full spin operators comprises 320 energy levels, the explicit consideration of which makes discussion of energies, spin states, and molecular properties and their relation to experiment possible.[66]

The ZORA BP86-D3 optimized structures were used for the eight required single-point calculations with the hybrid meta-GGA TPSSh density functional.[95] These calculations also employed the ZORA Hamiltonian, with larger ZORA-recontracted basis sets of def2-TZVP(-f) quality on all atoms[86,87] and fully decontracted def2-TZVP/J Coulomb fitting basis sets[90] along with the chain-of-spheres (RIJCOSX) approximation to the Coulomb and exchange terms.[96] Increased integration grids ("Grid4" and "GridX4" in ORCA convention) and tight SCF convergence criteria were used. Initial BS guesses were automatically constructed using the "flipspin" feature of ORCA. The overdetermined equation space from the high-spin and the seven BS solutions for the calculation of the six J constants were solved using singular value decomposition, which provides the best solution in the least-squares sense for the four spin center system. Having the six J constants for a given structure, it is straightforward to diagonalize the HDvV Hamiltonian to obtain the complete 320-level energy spectrum and hence to identify the correct ground spin state and calculate the associated properties of the model (see Supporting Information for details). The application of BS-DFT and the performance of TPSSh have been extensively discussed, benchmarked, and calibrated in recent studies of Mn systems.[66−68,70,72]

2.3. EPR Parameters. Isotropic hyperfine coupling constants A_{iso} were calculated for the manganese ions and coordinating nitrogens in each model, using the same methods (ZORA-TPSSh) as for the single-point calculations. Picture-change effects were applied to the calculation of hyperfine coupling constants (HFCs). The integration grids were increased to 11 and 9 (ORCA convention) for Mn and N centers, respectively. The theoretical approach follows previously established protocols that define a transformation of the "raw" value obtained from BS-DFT for a given nucleus K, $A^{(K)}_{\mathrm{iso,BS}}$, to values that can be compared to observable HFCs according to

$$A^{(K)}_{\mathrm{iso}} = \pm A^{(K)}_{\mathrm{iso,BS}}\left(\frac{\langle S_z\rangle_{\mathrm{BS}}}{S_A}\right)\left(\frac{\langle S_z^{(A)}\rangle}{S_t}\right) \tag{2}$$

S_t is the total spin (1/2 in the present case), and $\langle S_z\rangle_{\mathrm{BS}}$ is the total M_S of the BS wave function. Thus, the projection consists of adjusting

$A^{(K)}_{iso,BS}$ according to the ratio of the on-site spin expectation value $\langle S_z^{(A)}\rangle$ and the formal site spin S_A. The positive or negative sign refers to the majority (α) or minority (β) spin carried by the fragment. The on-site spin expectation value $\langle S_z^{(A)}\rangle$ that represents the coupling of the local spin of site A into the complicated multiconfigurational ground state wave function is obtained as

$$\langle S_z^{(A)}\rangle = \sum_{S_A M_{S_A} \ldots S_N M_{S_N}} |C_I^{S_A M_{S_A} \ldots S_N M_{S_N}}|^2 M_{S_A} \quad (3)$$

where $|C_I^{S_A M_{SA} \ldots S_N M_{SN}}|$ represents the weight of basis state I, $|S_A M_{S_A} \ldots S_N M_{S_N}\rangle$, in the ground state eigenfunction of the HDvV Hamiltonian $|S_A S_B \ldots S_{N-1} S_N S M_S\rangle$ with $M_S = S$. We refer the reader to the recent literature for a detailed theoretical treatment.[66] Since all current DFT functional implementations are known to systematically underestimate core spin polarization and hence HFCs as a function of the nuclear charge,[97−99] it is convenient to uniformly scale the final values by a factor appropriate to the given method to facilitate comparisons with experiment[53,66−68,98] (see Supporting Information, Table S1; 1.70 in the present case). ^{14}N HFCs were obtained and projected according to previously described procedures.[69]

3. RESULTS AND DISCUSSION

3.1. OEC Core Geometry and Ligand Environment. The protein environment of the inorganic OEC core in the Umena et al. 1.9 Å structure (3ARC)[19] is very similar to the structures obtained previously by Loll et al. (2AXT)[16] and Guskov et al. (3BZ1),[17] at 3.0 and 2.9 Å resolution, respectively. Multiple alignments of these structures[100−102] show that most backbone α-carbon atoms are found in similar positions, suggesting that the protein backbone has a consistent configuration and that the well-documented radiation damage to the cluster[23] does not propagate far from the inorganic core (see Supporting Information for details). On the other hand, the newly resolved positions of the metals in the 1.9 Å structure lead most importantly to a different assignment of the coordination mode of Asp170, which is now bridging Ca and the terminal Mn. The current assignment of the first and second coordination spheres of the Mn_4O_5Ca cluster is also in line with other experimental evidence.[103] However, the proposed connectivity within the inorganic Mn_4O_5Ca cluster appears unlikely on several grounds. First of all, the Mn−O distances in the crystallographic model are all unrealistically long, with an average distance of 2.1 Å, compared with typical distances in synthetic complexes, where bridging $Mn^{III/IV}$−O bond lengths are typically found within the range of 1.75−1.9 Å.[104−114] Indeed, the average of the Mn−O distances of the OEC was determined by EXAFS to be 1.85 Å, right in the middle of the experimentally well-established range for such bonds. Second-sphere interactions, explicitly considered in large QM-only and QM/MM computational models of Siegbahn and Batista, cannot explain Mn−O bond elongations that would result in such unprecedented distortions away from equilibrium bond lengths. The Mn···Mn distances in the crystallographic model are also a bit longer than those determined by EXAFS: the shortest Mn···Mn distance in the crystal structure is 2.8 Å, but this is known from EXAFS to be the longest of the three short Mn···Mn vectors (two of 2.7 Å, one of 2.8 Å).

These observations can be rationalized by the reference work of Yano et al.,[23] in which the X-ray dose was correlated with the percentage of Mn^{II}, the product of Mn photoreduction, in the sample. Under the conditions where the diffraction data for the 1.9 Å structure were collected, the amount of manganese that has been reduced by radiation to Mn^{II} is predicted to be approximately 25%

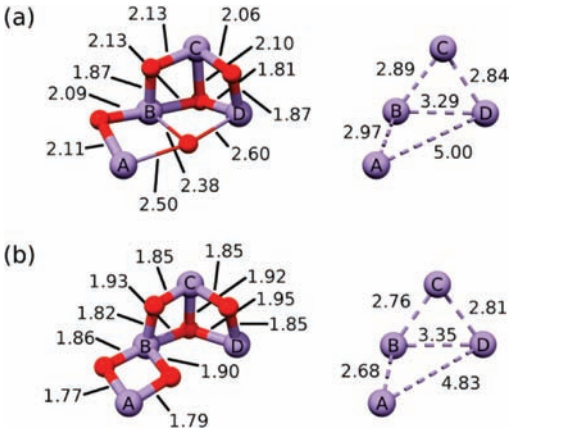

Figure 3. Mn μ-oxo (left) and Mn−Mn (right) interatomic distances for (a) the recent 1.9 Å crystal structure (3ARC) of Umena et al.[19] and (b) the fully optimized "parent" model **1**. Mn and O atoms are shown in purple and red, respectively. The Ca^{2+} cofactor has been omitted for clarity. All distances are in Ångströms.

according to the above correlations. In addition, a recent estimation of the oxidation state of Mn ions in the crystallographic model of Umena et al. by Grundmeier and Dau[115] based on the reported Mn−O bond lengths shows that the average oxidation state of Mn in the crystal should be +2.5, corresponding on average to a Mn(II, II,III,III) system rather than a pure S_1 state with Mn(III,III,IV,IV). It is clear, therefore, that at least part of the enzymes present in the Umena et al. crystal had OEC sites that are reduced even beyond the S_0 state, to nonphysiological negative states that lie outside the Kok cycle.[116,117] The presence of Mn^{II} and the coexistence of multiple cluster oxidation states in the crystal explain easily and convincingly the long distances deduced by the fitting of the diffraction data. Moreover, a direct calculation at the S_2 state of the unoptimized crystallographic OEC model reveals that O(5) is not bonded to either Mn_A or Mn_D and appears to be a "floating" radical center (Mulliken spin population ~0.7) that is incompatible with experiment. At the same time, the possibility of a protonated O(5) center is also unlikely, based on the absence of the expected strongly coupled proton hyperfine from ESEEM and ESE-ENDOR spectra of the OEC.[118]

Most importantly, relaxation of only the oxygen atoms in the inorganic core using the $Mn^{IV}_3Mn^{III}$ oxidation states (S_2 state) leads to an enormous energy stabilization of over 78 kcal mol^{-1} with concomitant shortening of Mn−O bonds to 1.8−1.9 Å, while further stabilization is gained with subsequent relaxation of the metal ions. This result is obtained with and without backbone constraints for models that explicitly include second-sphere residues, and it clearly demonstrates that the positions of the oxo bridges in the crystallographic model are far from optimal. In addition to the shortening of Mn−O bond lengths, the most important change upon optimization in terms of the bonding within the cluster is the shift of O(5) toward Mn_A to form a proper bond (1.8 Å) with this metal. This structural rearrangement results in placing the unique Mn^{III} of the S_2 state at Mn_D, which is now five-coordinate as expected for a Mn^{III} center and consistent with EPR spectroscopy.[41] Thus, the stretched "cuboid" part of the crystallographic model appears to be untenable and opens up upon energy minimization, leading to the creation of a bond between O(5) and Mn_A and of an empty coordination site on Mn_D. This opening of the assumed cuboid also proves to be crucial for achieving the experimentally

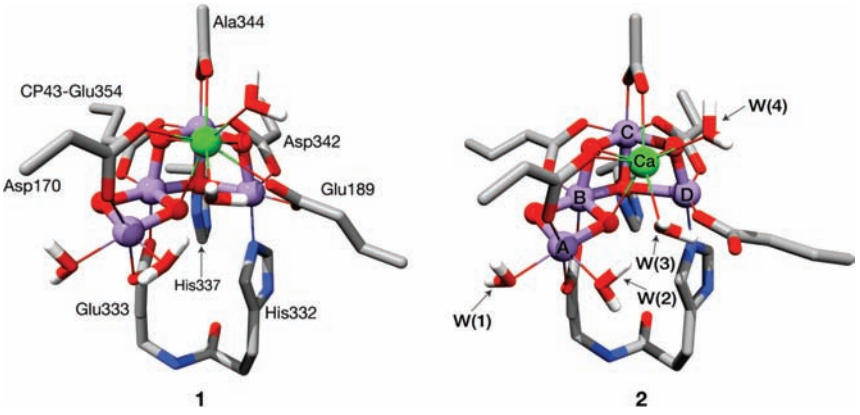

Figure 4. Two parent OEC models, **1** and **2**. Mn, Ca, N, O, C, and H atoms are shown in purple, green, blue, red, gray, and white, respectively. The labeling scheme for Mn and water ligand positions is shown for model **2** and is the same for model **1** and throughout the text. Hydrogen atoms other than those of the directly coordinating water molecules are omitted for clarity.

known low-spin ground state. A "closed" cuboid would necessarily lead to a different distribution of oxidation states placing the Mn^{III} ion at the dangler position. The Mn ions in a Mn_3O_4Ca cuboid are found to be ferromagnetically coupled due to the acute angles of the oxo bridges, which prohibit any superexchange interaction and impose a high spin ground state. This has been confirmed for other models incorporating a Mn_3O_4Ca cuboid, such as for example a model used by Sproviero et al.[54] This model is found to be incompatible with experiment for the S_2 state as it exhibits a spin 7/2 ground state due to the strong ferromagnetic Mn−Mn interactions imposed by the cubane geometry.

The thus optimized form of the Mn_4O_5Ca core is displayed in Figure 3b and compared to the crystallographic core geometry (Figure 3a). The Mn_4O_5Ca core topology that we derived here is not unprecedented in the literature. Starting from the latest crystal structure of PSII, the optimization appears to settle the issue of the exact core topology[119,120] in favor of the Mn_4O_5Ca core proposed by Siegbahn.[47,51] Indeed, the only major adjustment that needs to be done to the most recent complete Siegbahn model of the OEC to comply with the optimized crystallographic structure appears to be the replacement of a hydroxy bridge between Mn_A and Ca^{2+} with the bridging Asp170. Similar findings have been made by Kusunoki[63] and Luber et al.[121] starting as well from the new 1.9 Å crystal structure coordinates. A model proposed previously by Dau et al.[122] is also broadly similar but features a different connectivity pattern, the crucial difference from the present model being the orientation of the Jahn−Teller axis on Mn(III), aligned in that case along His332. It should be pointed out that the kind of "twisted-core" topology observed here is compatible with data obtained by polarized EXAFS spectroscopy, where this connectivity is featured in all proposed models.[27,28] Specifically, the present core is approximately a mirror image of the polarized EXAFS model III in the original paper,[27] having otherwise the same bonding pattern and distribution of Mn···Mn distances (Figure S6, Supporting Information). Compared with older crystallographic models, the present model agrees very well with the "Berlin" structure,[16−18] whereas the original "London" structure[14] differs substantially in arrangement, orientation, and even the precise stoichiometry of the inorganic core (see Supporting Information for detailed comparisons), having apparently suffered significantly more radiation damage than subsequent crystallographic models.

There is ample additional evidence that such a model best approximates the OEC, not only on structural but also on energetic,[123] mechanistic,[34,47] and spectroscopic grounds.[53,67] Most recent support was provided by a thorough analysis of the effects of Ca^{2+}/Sr^{2+} substitution on multifrequency simulations of X- and Q-band cw-EPR and Q-band ^{55}Mn pulsed ENDOR spectra.[41] Therefore, the refinement of the Umena et al. crystallographic model into a form where the bonding in the Mn_4O_5Ca core agrees with that of the Siegbahn model forms the basis for constructing our starting models and all the subsequent protonation variants that will be evaluated in the following.

3.2. Optimized Geometries and Relative Energies. In the previous section, we showed how the most recent crystal structure of the OEC core must be refined to obtain an energy-minimized model that is compatible with EXAFS. Within the coordination environment described above, there are four waters of undefined protonation states in the structure, two on Mn_A and two on the Ca^{2+} cofactor.[19] The possibility of a third water molecule coordinated to Ca^{2+} was investigated, but it was found to dissociate and only remain hydrogen-bonded to the cluster. We have proceeded with geometry optimizations of a large number of input structures that differed in details such as the orientation of waters, the orientation of the Jahn−Teller axis of Mn^{III}, as well as the hapticity and rotation of the amino acid side chains. This effort led us to converge to two similar but distinct minima, the "parent" structures **1** and **2** (Figure 4) that differ mainly in the coordination mode of Glu189. From these two structures, the large set of permutations used in the present study were subsequently generated by proton shifts and removals.

Overall, four classes of models were considered. Each structure included the directly coordinating residues, Asp170, Glu189, His332, Glu333, Asp342, and Glu354, from the CP43 pigment protein complex (CP43−Glu354) and the C-terminus Ala344, plus the nearby His337 that hydrogen bonds to the μ_2-oxo bridge between Mn_C and Mn_D (Figure 4).[17] The first class consisting of models **1** and **2** included four water molecules, two coordinated to Mn_A and two to the Ca^{2+} cofactor (see Figure 4). The second class of models investigated the possibility of protonation of the μ-oxo bridge, O(5), between Mn_A and Mn_B because it is suggested that this bridge is derived from a substrate water molecule that binds during the S_4 to S_0 transition (see Figure 1).[34,51] Therefore, depending on the deprotonation sequence, this bridge may be singly protonated in the S_2 state. Protonation of the second μ-oxo bridge between Mn_A and Mn_B was not considered due to clashes with nearby residues within the crystal structure. For the models

dx.doi.org/10.1021/ja2041805 |J. Am. Chem. Soc. 2011, 133, 19743–19757

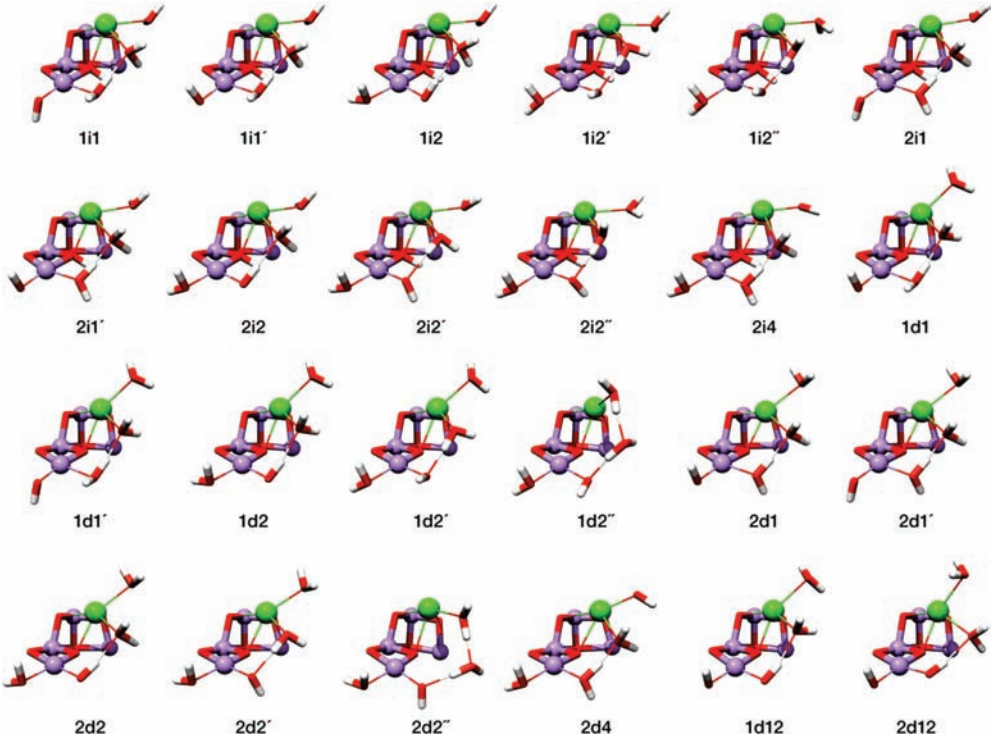

Figure 5. Protonation patterns considered in the present study. For clarity, the amino acid ligands are not shown. Mn, Ca, O, and H atoms are shown in purple, green, red, and white, respectively. In labels "*min*" and "*mdn*" *m* indicates the parent model from which the model was constructed (**1** or **2**; Figure 4); *n* indicates the specific water deprotonation site; and i or d indicates proton-shift isomers and deprotonated derivatives of the parent models, respectively.

used here, these nearby residues have not been included. Each model was constructed as an isomer of the parent models **1** and **2** through a selective proton shift from a coordinated water molecule. This procedure resulted in 11 structurally stable models, for which we will use the nomenclature "***min***" where *m* gives the parent model from which the isomer was constructed (*m* = **1** or **2**) and *n* indicates the specific water molecule that was deprotonated. Care was taken to only remove hydrogen atoms that are not involved in hydrogen bonds. In situations where significantly different structures and/or hydrogen bond networks were produced upon geometry optimization, the different minima are indicated by primes; for example, models **2i2**, **2i2**′, and **2i2**″ differ in their hydrogen bonding networks and location of water ligands (see Figure 5). A similar procedure was used in the construction of singly deprotonated structures, resulting in a series of models labeled similarly as "***mdn***". Finally, the fourth class of models was constructed by deprotonating two water molecules. The resulting structures are labeled **1d12** and **2d12**, indicating that protons are removed from waters W(1) and W(2) on Mn_A (see Figures 4 and 5). Different proton-shift and deprotonation possibilities including deprotonation of calcium-bound waters were explored and will be discussed in the following. Of the several tens of models investigated, only those that proved structurally stable are discussed below.

This study has been restricted to models with charges of +1, 0, and −1, as we consider it unlikely that the existing pocket could compensate for a higher core charge, either positive or negative. The parent structures and isomers are positively charged; the singly deprotonated variants are neutral; and the doubly deprotonated models have a negative charge. It is noted that the structures of the final set of models used for calculations of spectroscopic parameters were freely optimized.

The geometries for the 26 models all show a well-defined "fused-twisted" core[67] with a $Mn_{A,B}$ dimer-like unit attached at Mn_B to a fused $Mn_{B,C,D}$ trimer. In all models Mn_D, Mn^{III}, is five-coordinate in a square pyramidal geometry, and the three Mn^{IV} are six-coordinate. For models based on parent structure **1**, the pseudo-Jahn−Teller axis is along the Mn_D−Asp342 bond with the open coordination site facing an $Mn_{A,B}$ μ-oxo bridge, whereas for all models based on structure **2**, the Jahn−Teller axis is instead along the MnD−μ_3-oxo bond. This is a consequence of the differing coordination mode for Glu189 between models **1** and **2**. Within model **1**, Glu189 is a bridging ligand between Mn_D and Ca^{2+}, but in model **2** the side chain is rotated such that it hydrogen bonds to the calcium-coordinated water W(3) instead of coordinating to Ca^{2+}. This rotation results in the previously mentioned different Jahn−Teller axis orientations in the two models, as well as in a consistently larger $Mn_B \cdots Mn_D$ separation by ca. 0.2 Å for geometries based on parent model **2** (see below).

The differences in the coordination sphere of Mn_D have important consequences for the calculated exchange coupling constants, spin ladder, and effective ground state spin (S_t) of the models which will be discussed in more detail in later sections. Attempts to complete the octahedral coordination sphere of Mn_D, through the addition of an extra water molecule in the empty site, proved to be unsuccessful. In both types of models, **1** or **2**, the extra water molecule did not remain coordinated to Mn_D upon geometry optimization.

It was found during optimization that, for all models, the possibility of an OH^- ligand to Ca^{2+} residing at water position 3 was not possible. Each initial starting geometry containing an OH^- at position 3 converged to a final geometry wherein the OH^- was located in ligand position 2, by proton transfer from

Table 1. Selected Interatomic Distances (Å) and Relative Energies ΔE (kcal mol^{-1}) for Optimized Models

total charge	model	Mn_A-Mn_B	Mn_B-Mn_C	Mn_C-Mn_D	Mn_B-Mn_D	$Mn_{A,B,C,D}-Ca$	ΔE^a
+1	**1**	2.68	2.76	2.81	3.35	3.75, 3.43, 3.28, 3.58	0.0
	1i1	2.84	2.76	2.79	3.39	3.95, 3.47, 3.27, 3.79	6.6
	1i1′	2.83	2.76	2.80	3.39	3.95, 3.48, 3.27, 3.79	5.4
	1i2	2.82	2.76	2.79	3.36	3.90, 3.51, 3.28, 3.81	12.7
	1i2′	2.80	2.75	2.79	3.35	3.83, 3.52, 3.28, 3.80	10.4
	1i2″	2.80	2.75	2.80	3.36	3.84, 3.53, 3.27, 3.76	11.7
	2	2.68	2.75	2.87	3.62	3.75, 3.39, 3.26, 3.46	0.5
	2i1	2.85	2.76	2.83	3.59	3.98, 3.45, 3.25, 3.69	8.3
	2i1′	2.84	2.76	2.83	3.59	3.98, 3.46, 3.26, 3.69	6.7
	2i2	2.83	2.76	2.82	3.57	3.92, 3.50, 3.27, 3.72	13.5
	2i2′	2.82	2.75	2.82	3.57	3.90, 3.52, 3.28, 3.47	10.5
	2i2″	2.81	2.75	2.81	3.59	3.88, 3.51, 3.24, 3.73	14.0
	2i4	2.80	2.74	2.83	3.56	4.12, 3.70, 3.36, 3.70	37.2
0	**1d1**	2.71	2.78	2.79	3.33	3.77, 3.34, 3.26, 3.52	0.6
	1d1′	2.71	2.78	2.79	3.33	3.77, 3.33, 3.26, 3.53	2.1
	1d2	2.70	2.78	2.79	3.31	3.71, 3.41, 3.28, 3.53	4.2
	1d2′	2.69	2.77	2.79	3.33	3.72, 3.45, 3.31, 3.56	0.0
	1d2″	2.70	2.77	2.80	3.26	3.69, 3.40, 3.25, 3.56	1.2
	2d1	2.71	2.77	2.86	3.61	3.78, 3.31, 3.25, 3.46	3.5
	2d1′	2.72	2.77	2.86	3.60	3.78, 3.31, 3.25, 3.46	5.5
	2d2	2.70	2.77	2.86	3.60	3.70, 3.39, 3.27, 3.46	6.7
	2d2′	2.70	2.76	2.86	3.61	3.69, 3.39, 3.28, 3.47	1.3
	2d2″	2.71	2.77	2.82	3.21	3.75, 3.38, 3.20, 3.53	3.0
	2d4	2.68	2.75	2.85	3.60	3.92, 3.58, 3.37, 3.51	24.2
−1	**1d12**	2.74	2.79	2.79	3.29	3.76, 3.31, 3.25, 3.47	1.5
	2d12	2.73	2.80	2.80	3.32	3.72, 3.33, 3.21, 3.49	0.0
	Exp.[b]		2.7, 2.8 (2:1)		3.2	3.4, 3.9 (2:2 or 3:1)	

[a] Relative energies shown are for sets of models with the same charge (+1, 0 or −1). [b] Distances obtained from EXAFS studies.[11,28]

W(2) to the OH^- ligand in position 3. Similar results were observed for most models with OH^- ligands in position 4. Here, however, the proton transfer was completed in two steps during geometry relaxation, first through a transfer of a proton from W(3) to the OH^- ligand in position 4 and then a subsequent transfer from W(2) to the OH^- ligand now in position 3. These observations suggest that the role of the Ca^{2+} cofactor is not to stabilize an OH^- ligand in the water oxidation cycle. In the S_2 state, only the energetically unfavorable models **2i4** and **2d4** contain an OH^- ligand on the Ca^{2+} cofactor after optimization. For the models studied, structures with OH^- ligand(s) on Mn_A were found to best represent stable geometries of the OEC.

Table 1 shows selected interatomic distances for all of the models in comparison to measured EXAFS distances for the Mn_4O_5Ca cluster in the S_2 state.[11,28] All constructed models broadly follow the general pattern of the EXAFS data set in terms of the distribution of short and long distances, but certain deviating results are apparent. Specifically, models derived from structure **2** have a $Mn_B\cdots Mn_D$ interatomic distance that is 0.3 Å larger, on average, than that of models derived from structure **1**. Thus, models of type **2** significantly overestimate the long Mn···Mn distance determined by EXAFS. The alternate orientation of Glu189 within the type **2** models necessitates this longer interatomic distance due to the reorientation of the Jahn−Teller axis along the $Mn_D-\mu$-oxo bond. As can be expected, protonation of the $Mn_{A,B}-\mu$-oxo bridge leads to an elongation of the $Mn_A\cdots Mn_B$ interatomic distance of approximately 0.1 Å within the isomer models. Interestingly, the deprotonation of the water ligands W(1) and W(2) on Mn_A also leads to an increase in the $Mn_A\cdots Mn_B$ interatomic distance. However, this increase is an order of magnitude smaller, at approximately 0.02−0.03 Å. With respect to the four Mn···Ca distances, the results in Table 1 indicate that in all models a long distance of 3.8−3.9 Å always corresponds to $Mn_A\cdots Ca$, whereas the distances of Mn_B and Mn_C from Ca^{2+} are consistently shorter, ca. 3.4 Å for $Mn_B\cdots Ca$ and 3.3 Å for $Mn_C\cdots Ca$. These three distances can therefore be considered consistent with the long and short distances reported from EXAFS. The $Mn_D\cdots Ca$ distance is more variable and appears to depend on the overall protonation state and charge of the model. Thus, it is generally close to 3.8 Å for most of the **1*in*** and **2*in*** series, while it contracts to ca. 3.5 Å for the deprotonated models. Thus, although it cannot be decided at this point whether a 3:1 or 2:2 ratio of short-to-long Mn···Ca distances is to be expected for the S_2 state, the results fall indeed within the two most probable EXAFS-determined ratios. We expect that this issue will be better clarified in future models that will be expanded to include the region of the system extending from Ca^{2+} to Tyr161 (Y_Z) and its immediate environment.

Relative energies for the optimized models are calculated at the same level of theory as the EPR parameter calculations.[82] In Table 1, energies have been compared between groups of the same class, i.e., parent models and isomers, singly deprotonated and doubly deprotonated. Estimates for the relative energies between classes show that the singly deprotonated models are approximately 6 and 19 kcal mol^{-1} lower in energy than the

Table 2. Calculated Exchange Coupling Constants J (cm^{-1}), Total Spin of Ground (GS) and First Excited States (ES), and Energetic Separation of the Two Lowest Energy Levels (cm^{-1}) for the Parent Structures and Their Proton-Shift Isomers

model	J_{AB}	J_{AC}	J_{AD}	J_{BC}	J_{BD}	J_{CD}	S_t (GS)	S_t (ES)	ΔE_{ES-GS}
1	−8	2	2	17	−1	−17	1/2	3/2	18
1i1	−11	1	1	14	−10	−22	1/2	3/2	27
1i1′	−10	1	1	14	−10	−22	1/2	3/2	24
1i2	−12	2	0	13	−11	−23	1/2	3/2	27
1i2′	−7	2	1	13	−13	−21	1/2	3/2	17
1i2″	−8	2	1	13	−14	−20	1/2	3/2	17
2	−10	1	0	15	−23	11	7/2	5/2	—
2i1	−17	1	0	14	−22	10	7/2	5/2	—
2i1′	−15	1	0	14	−23	10	7/2	5/2	—
2i2	−15	2	0	11	−20	9	7/2	5/2	—
2i2′	−17	2	0	13	−23	12	7/2	5/2	—
2i2″	−18	2	0	14	−20	10	7/2	5/2	—
2i4	−9	2	−1	14	−27	17	7/2	5/2	—
Exp.[a]	—	—	—	—	—	—	1/2	3/2	13−22

[a] Ground state spin and first excitation energy gap determined from EPR measurements on *T. elongatus*.[34,40]

Table 3. Calculated Exchange Coupling Constants J (cm^{-1}), Total Spin of Ground (GS) and First Excited States (ES), and Energetic Separation of the Two Lowest Energy Levels (cm^{-1}) for the Singly and Doubly Deprotonated Models

model	J_{AB}	J_{AC}	J_{AD}	J_{BC}	J_{BD}	J_{CD}	S_t (GS)	S_t (ES)	ΔE_{ES-GS}
1d1	−16	1	2	20	6	−21	1/2	3/2	25
1d1′	−17	1	2	20	6	−21	1/2	3/2	25
1d2	−15	3	4	16	3	−21	1/2	3/2	27
1d2′	−14	2	3	16	1	−20	1/2	3/2	26
1d2″	−11	3	7	17	2	−21	1/2	3/2	22
2d1	−21	1	0	17	−18	5	1/2	3/2	4
2d1′	−22	1	0	18	−18	4	1/2	3/2	5
2d2	−14	2	−1	13	−15	3	1/2	3/2	4
2d2′	−17	2	−1	13	−18	7	7/2	5/2	—
2d2″	−18	4	10	18	5	−22	1/2	3/2	28
2d4	−10	1	0	15	−26	12	7/2	5/2	—
1d12	−14	1	2	18	8	−25	1/2	3/2	22
2d12	−9	1	2	19	9	−27	1/2	3/2	13
Exp.[a]	—	—	—	—	—	—	1/2	3/2	13−22

[a] Ground state spin and first excitation energy gap determined from EPR measurements on *T. elongatus*.[34,40]

parent/isomer and doubly deprotonated models, respectively, as taken from a comparison of the lowest energy models for each set (**1**, **1d2′**, and **2d12**). The calculated relative energies for models **1** and **2** show that even given the large differences in the coordination environment of Mn_D the structures have effectively the same energies. The isomers of **1** and **2** (series **1i*n*** and **2i*n***) have energies at least 5 kcal mol^{-1} higher than those of the parent models, suggesting that the protonation of the $Mn_{A,B}$−μ-oxo bridge (see Figure 5) is unfavorable. It is noteworthy that a clear distinction can be made for the energy cost of deprotonating either W(1) or W(2) of Mn_A. Specifically, a proton shift from W(1) to the oxo bridge is always favored (models **1i1**, **1i1′**, **2i1**, and **2i1′**) over deprotonation of W(2). The **1i2** and **2i2** series are uniformly more than 10 kcal mol^{-1} higher in energy than their parent structures. The most significant deviation is for that of model **2i4**, which is 37 kcal mol^{-1} higher in energy than the parent model. This presents further evidence that in the S_2 state the calcium cofactor does not perform a stabilizing role for a hydroxide to be used later in the reaction cycle.

Singly deprotonated models have calculated energies that favor models of type **1**, **1d1** and **1d2′** being the most stable and practically isoenergetic structures. In contrast to the situation with the proton-shift isomers, the singly deprotonated models of the **1d*n*** and **2d*n*** series display a much narrower range of energies. The details of the hydrogen-bonding network, such as the relative orientations of the OH^- group on Mn_A and water W(3) on Ca^{2+}, clearly affect the relative energies of the models but not enough to provide clear-cut distinctions. As will be discussed below, the spectroscopic properties of these models offer an additional criterion to differentiate among them; however, it is conceivable that an equilibrium involving similar protonation states could be operative in the natural system at ambient temperatures.[62,63,124,125] Model **2d4**, which bears a hydroxy ligand on calcium, again stands out from this set of isomers for being more than 24 kcal mol^{-1} higher in energy than the most stable species **1d2′**. It should be noted that water W(3) is practically dissociated from calcium in models **1d2″** and **2d2″** and is only kept in place by hydrogen bonds to the hydroxyl on Mn_A and the fourth water molecule, W(4), on Ca^{2+}.

From the results presented above, the models that arise as best candidates based on EXAFS distances and energetic considerations are **1**, **1d1**, **1d1′**, **1d2**, **1d2′**, **1d2″**, **2d2″**, **1d12**, and **2d12**. Nevertheless, to obtain a complete picture of the interplay between protonation patterns and properties of the clusters, the electronic structures of all models were calculated and are analyzed below.

3.3. Exchange Couplings and Ground States. The exchange coupling constants, J_{ij}, effective ground state S_t, and the spin ladder were calculated within the BS-DFT formalism described in the Computational Methods section (see also Supporting Information). Below models of the same class (parent and isomers, singly deprotonated, and doubly deprotonated models) are discussed separately.

3.3.1. Parent Models and Isomers. Table 2 shows the exchange coupling constants, J_{ij}, between the four Mn spin centers calculated using the BS-DFT formalism. All models show antiferromagnetic coupling between Mn_A and Mn_B and ferromagnetic coupling between Mn_B and Mn_C. The series demonstrates how the subtle interplay between the nature of the ligands (oxo or hydroxo) and the orientation of the hydrogen-bonding network modulate the exchange coupling constants for specific manganese pairs. Regarding the reliability of the present methods, it is useful to note that the J_{AC} and J_{AD} couplings may serve as an indication of the numerical stability of the method: they are always close to zero, as can be anticipated from qualitative topological arguments.[34] Models of type **1** differ from those of type **2** in the nature of the coupling between Mn_C and Mn_D: in the former this coupling is calculated as antiferromagnetic, whereas in the latter the coupling is strictly ferromagnetic. This appears to be the decisive factor that leads to effective ground state spins of $S_t = 1/2$ and $S_t = 7/2$ for models of type **1** and **2**, respectively. Experimentally, the effective ground state spin of the S_2 state is $S_t = 1/2$; therefore, isomer models of **1** can be

considered as good candidates, whereas isomers of **2** can probably be discarded from further consideration, reinforcing the conclusions drawn above based on EXAFS-derived metal−metal distances and comparison of relative energies.

The calculated energy gaps between the spin doublet ground state and the first $S_t = 3/2$ excited state for **1** and the **1*in*** models are comparable to experimental estimates ($13-22\ cm^{-1}$).[40] As discussed recently, the energy separation between the ground and first excited electronic states for the S_2 state differs between species and is also enhanced to a different extent by addition of MeOH.[40] Since the present models do not explicitly include MeOH, a degree of uncertainty can be considered with regard to the experimental reference. Given that an atomic-level understanding of the MeOH interaction is lacking and even the origin of the inherent differences between species is uncertain, it appears prudent at this stage to use these values only as a guide and avoid overinterpretations.

3.3.2. Singly Deprotonated Models. The calculated exchange coupling constants for singly deprotonated models are shown in Table 3. Of note is the increase in the antiferromagnetic coupling between Mn_A and Mn_B upon deprotonation of either W(1) or W(2). In the case of type **1** models, this leads to a slight increase in the calculated energy gap between the ground state and the first excited state. For models of type **2**, the increase in the antiferromagnetic coupling between Mn_A and Mn_B leads to an $S_t = 1/2$ ground state with a small calculated ground state to first excited state energy gap ($1-5\ cm^{-1}$). Singly deprotonated type **1** models, however, have calculated energy separations that are close to $25\ cm^{-1}$. It is thus expected that the energy separation between the ground and first excited state is regulated by factors that influence the type, magnitude, and balance of the coupling between Mn_D and Mn_B/Mn_C (J_{BD}, J_{CD}).

Model **2d2″** presents a special case for the type **2** models in that the Jahn−Teller axis is no longer in the direction of the μ-oxo but instead is reoriented along the Asp342, similar to the type **1** models. The Glu189 residue, however, is hydrogen bonded to W(3) and is not coordinated to the Ca, as is the case for model **1**. This structural change leads to calculated exchange coupling constants and energetic spin ladders similar to those of type **1** models, namely, an energy separation of $28\ cm^{-1}$ versus energy separations of $22-27\ cm^{-1}$ for structures derived from model **1**.

One model (**2d4**) contains an OH ligand in position 4, coordinated to the Ca^{2+} cofactor. Model **2d4** also has a similar change in the location of the Glu189 residue as that of **2d2″**, but as the OH ligand is not located on Mn_A the ground state is not spin 1/2 and is instead spin 7/2. Here the coordination of the OH^- to Ca^{2+} instead of Mn_A does not stabilize the effective spin 1/2 ground state as is seen in the other type **2** singly deprotonated models. Indeed, the calculated exchange coupling constants for model **2d4** are essentially identical to those of the parent model **2**.

3.3.3. Doubly Deprotonated Models. Calculated exchange coupling constants for models with two OH^- ligands on Mn_A are presented in Table 3. Model **2d12** is structurally similar to model **2d2″** in that the Jahn−Teller axis is no longer in the direction of the μ-oxo but instead is along the Asp342, similar to the type **1** models. In **2d12**, like **2d2″**, the Glu189 residue is hydrogen bonded to W(3) and is not coordinated to the Ca, as is the case for model **1**. This structural change, as was commented on before for model **2d2″**, leads to calculated exchange coupling constants and energetic spin ladders similar to those of model **1**. Here, however, for both **1d12** and **2d12** the calculated energy gap between the ground state of spin 1/2 and the first excited state of spin 3/2 is reduced over models with only a single OH^- ligand on Mn_A, i.e., **1d1**, **1d1′**, **1d2**, **1d2′**, and **1d2″**. Note that the deprotonation of the second water on Mn_A in **1d12** does not significantly perturb the exchange couplings compared to practically all **1d1** and **1d2** models. Nevertheless, as will be shown below, this second deprotonation has a large impact on the spectroscopic properties.

Table 4. Computed On-Site Spin Expectation Values for the Four Mn Centers

model	topology	$\langle S_z^{(A)} \rangle$	$\langle S_z^{(B)} \rangle$	$\langle S_z^{(C)} \rangle$	$\langle S_z^{(D)} \rangle$
1	$\alpha\beta\beta\alpha$	0.751	−0.496	−0.432	0.677
1i1	$\alpha\beta\beta\alpha$	0.789	−0.478	−0.406	0.595
1i1′	$\alpha\beta\beta\alpha$	0.797	−0.471	−0.397	0.571
1i2	$\alpha\beta\beta\alpha$	0.800	−0.473	−0.375	0.548
1i2′	$\alpha\beta\beta\alpha$	0.818	−0.441	−0.364	0.486
1i2″	$\alpha\beta\beta\alpha$	0.817	−0.441	−0.372	0.496
1d1	$\alpha\beta\beta\alpha$	0.361	−0.339	−0.499	0.977
1d1′	$\alpha\beta\beta\alpha$	0.396	−0.364	−0.500	0.968
1d2	$\alpha\beta\beta\alpha$	0.577	−0.461	−0.480	0.864
1d2′	$\alpha\beta\beta\alpha$	0.635	−0.485	−0.472	0.823
1d2″	$\alpha\beta\beta\alpha$	0.666	−0.494	−0.466	0.794
2d1	$\alpha\beta\beta\alpha$	0.551	−0.492	−0.489	0.930
2d1′	$\alpha\beta\beta\alpha$	0.552	−0.491	−0.490	0.929
2d2	$\alpha\beta\beta\alpha$	0.646	−0.500	−0.500	0.854
2d2″	$\alpha\beta\beta\alpha$	0.565	−0.458	−0.488	0.882
1d12	$\alpha\beta\beta\alpha$	0.143	−0.155	−0.487	1.000
2d12	$\alpha\beta\beta\alpha$	0.125	−0.143	−0.481	0.999

3.4. Spin Expectation Values and ^{55}Mn Hyperfine Coupling Constants. The on-site spin expectation values for each complex with an effective spin of $S_t = 1/2$ are shown in Table 4, along with the corresponding broken-symmetry spin topologies. All models exhibit the "$\alpha\beta\beta\alpha$" topology, with positive signs of the site spin expectation values for Mn_A and Mn_D and negative signs for Mn_B and Mn_C. The values fall into three categories: (a) those that have the largest spin expectation value on Mn_A, (b) those that have the largest spin expectation value on Mn_D, and (c) those with very small values for Mn_A and Mn_B. The first category contains model **1** and its isomers, which have large on-site expectation values for Mn_A. This is somewhat unexpected for a Mn^{IV} ion based on typical simulations of mixed-valent $Mn^{III}Mn^{IV}$ dimer complexes.[37,126−128] In the following, the more commonly referred to isotropic spin projections of each Mn center, which are simply twice the calculated on-site spin expectation values for ground state spin 1/2 systems, are discussed.

The second category, which includes all **1d** and **2d** models with the exception of the doubly deprotonated **1d12** and **2d12**, conforms to the expected spin projection pattern from a comparison of experimental Mn dimer systems; i.e., the highest spin projection is found on the Mn^{III} ion. An experimental estimate for the spin projection of the Mn that is coordinated to His332 (Mn_D in our models) has been reported by Britt and coworkers.[129] It was estimated that the spin projection was approximately 2.0 from comparison of the measured ^{14}N hyperfine coupling to that of Mn model complexes. This suggests that this second category in which the relative spin projections follow a pattern of approximately 1.0, −1.0, −1.0, and 2.0 includes models of the correct protonation pattern. The only models

dx.doi.org/10.1021/ja2041805 |*J. Am. Chem. Soc.* 2011, 133, 19743–19757

Table 5. Calculated Spin-Projected ^{55}Mn Isotropic Hyperfine Coupling Constants (MHz), Compared with Absolute Values from Experiment

model	redox states	$A_{iso}^{(A)}$	$A_{iso}^{(B)}$	$A_{iso}^{(C)}$	$A_{iso}^{(D)}$
1	IV−IV−IV−III	−345.4	213.9	174.2	−192.4
1i1	IV−IV−IV−III	−342.7	184.0	163.0	−183.9
1i1′	IV−IV−IV−III	−345.6	181.6	159.0	−176.8
1i2	IV−IV−IV−III	−369.5	182.0	152.6	−167.5
1i2′	IV−IV−IV−III	−377.2	176.0	146.6	−155.9
1i2″	IV−IV−IV−III	−376.3	176.0	150.1	−177.0
1d1	IV−IV−IV−III	−166.5	133.0	207.4	−254.9
1d1′	IV−IV−IV−III	−183.0	142.4	207.8	−251.2
1d2	IV−IV−IV−III	−266.3	180.5	201.5	−217.5
1d2′	IV−IV−IV−III	−291.6	201.1	195.3	−208.4
1d2″	IV−IV−IV−III	−303.3	203.5	193.1	−219.1
2d1	IV−IV−IV−III	−227.7	165.3	170.2	−276.2
2d1′	IV−IV−IV−III	−229.6	164.1	170.8	−277.2
2d2	IV−IV−IV−III	−268.9	173.8	175.3	−256.1
2d2″	IV−IV−IV-III	−227.0	161.6	178.4	−207.8
1d12	IV−IV−IV−III	−67.6	56.0	210.1	−237.1
2d12	IV−IV−IV−III	−59.3	52.0	205.3	−251.9
Exp.[a,b]		191	208	251	312
Exp.[a,c]		193	205	248	298
Exp.[a,d]		200	217	245	297

[a] Values from experiment are listed in increasing order and do not correspond to any particular Mn atom. [b] From ref 41. [c] From ref 34. [d] From ref 37.

which satisfy this pattern are those which have a single deprotonation of either W(1) or W(2) on Mn_A and a total charge of zero. It is intriguing that the isomer models such as **1i1** and **2i2**, which do have an OH^- ligand on Mn_A, do not exhibit the same calculated on-site expectation values. This is most likely due to the magnitude of the exchange coupling between Mn_A and Mn_B. It has been noted previously[34,67] that the magnitude of this coupling is a crucial parameter for the OEC, largely determining the effective ground state for models of this metal-ion topology as can be seen in Tables 2 and 3, as well as the on-site spin expectation pattern.

The third category of on-site spin expectation values, those giving a spin projection pattern of approximately 0.1, −0.1, −1.0, and 2.0, falls into the hypothesized projection pattern put forward by Petrie, Stranger, and Pace.[130,131] These are the doubly deprotonated models, **1d12** and **2d12**, both of which contain only OH^- ligands on Mn_A. An exploration of the calculated ^{55}Mn hyperfine components, both the intrinsic (Table S2, Supporting Information) and projected (Table 5), respectively, argue against these models. To reproduce EPR and ^{55}Mn-ENDOR data simultaneously, such a model would require the two manganese ions which make up the dimer unit carrying the unpaired electron spin (Mn_C−Mn_D) to have two additional properties not yet observed in manganese model complexes: (a) the magnitude of the onsite hyperfine tensor for the Mn^{III} (Mn_D) would have to be approximately two times that previously observed and (b) the effective hyperfine tensor anisotropy for the Mn^{IV} (Mn_C) would also have to be unusually large. The former is required to reproduce the inhomogeneous line width of the EPR "multiline" spectrum. The latter is a consequence of the first criterion as the ^{55}Mn-ENDOR signal of the Mn^{III} would appear at very large radio frequencies, above those currently measured, i.e., in excess of 500 MHz. Thus, the entire ^{55}Mn-ENDOR signal that is observed would have to be assigned to Mn_C. This would require the hyperfine tensor of Mn_C in the coupled representation to be highly anisotropic. While the anisotropy of the hyperfine tensors in the coupled representation is in part a property of the coupled system as opposed to the individual Mn, it is highly unlikely that an exchange coupling topology exists that could confer such a large hyperfine anisotropy. It would require a very large on-site fine structure tensor (**D**) for the Mn^{III} ion, outside the range seen in model complexes.[41] Thus, the dimer of dimers model has all but been excluded as a feasible model for the electronic structure of the OEC.

Table 5 collects all the calculated spin-projected isotropic ^{55}Mn hyperfine coupling constants for models with the correct ground spin state. Intrinsic site values are reported in Table S3 of the Supporting Information. For a comparison to experimental values, the absolute magnitude of the calculated hyperfine coupling constants is used. Additionally, it should be noted that the experimental hyperfine coupling constants are not site specific. As such, the comparison between the calculated values and experimental values is made for each set of calculated hyperfine coupling constants to the set of experimental values, neglecting the origin of the calculated values.

It is readily observed that only the singly deprotonated models **1d2′** and **1d2″** give values that are fully consistent with experiment. As can be anticipated from inspection of the on-site expectation values, model **1** and its isomers (**1i*n*** series) as well as the doubly deprotonated models **1d12** and **2d12** cannot be considered as good models of the OEC, both structurally and electronically. The latter result is surprising, as it was not observed in our earlier study.[67] In this earlier work, a modified Siegbahn model (model 11 in that study) was examined.[51] This model had two hydroxyl ligands on Mn_A, i.e., a doubly deprotonated model. It was shown to yield good estimates for the onsite spin expectation values and, as a consequence, reasonable projected ^{55}Mn-hyperfine couplings. Inspection of the exchange coupling topology for this earlier model and that of models **1d2′**, **1d2″**, **1d12**, and **2d12** reveals that all four models only differ by the exchange pathways J_{AD} and J_{BD}. Variation of J_{AD} is essentially facile, whereas small changes in J_{BD} (<5 cm^{-1}) switch the onsite spin expectation values from "tetramer-like", where all four values are similar, to "dimer of dimers like", for which two values (Mn_A and Mn_B) are close to zero. For example, if J_{BD} is decreased from 8 to 4 cm^{-1} for model **1d12**, the onsite spin expectation values become [0.54, −0.44, −0.49, 0.89]. Assuming the onsite hyperfine couplings to be identical for this modified coupling topology, the resultant projected hyperfine couplings are [−256, 159, 211, and −211] MHz, which is much more in line with values seen experimentally. Thus, while it is tempting to completely exclude the doubly deprotonated models, further work must be performed before this statement can be made, especially as there is no clear mechanism how the protonation state of the ligands of Mn_A propagates through the superexchange network.

As a final note, it is observed that for the models **1d2′** and **1d2″**, which show the best agreement with ^{55}Mn EPR/ENDOR in their current construction, the largest ^{55}Mn hyperfine tensor is not assigned to the Mn^{III} (Mn_D) but instead to a Mn^{IV} (Mn_A). This is in contrast to all experimentally derived models of the electronic structure of the OEC in the S_2 state. These models were in part based on comparison with mixed valence models (Mn^{III}/Mn^{IV}, $Mn^{II}Mn^{III}$) in which the largest projected hyperfine coupling can always be assigned to the M_n of highest intrinsic spin, in

Table 6. Overview of Investigated Model Properties: Qualitative Agreement of All Models with Respect to Structural, Energetic, and Spectroscopic Criteria Is Indicated As Good (+), Sufficient (o), or Poor (−)

model	geometry	relative energy	spin state	energy gap	spin projections	^{55}Mn HFCs
1	+	+	+	+	o	o
1i1	o	o	+	+	−	−
1i1′	o	o	+	+	−	−
1i2	+	−	+	+	−	−
1i2′	+	−	+	+	−	−
1i2″	+	−	+	+	−	−
2	−	+	−			
2i1	−	o	−			
2i1′	−	o	−			
2i2	−	−	−			
2i2′	−	−	−			
2i2″	−	−	−			
2i4	−	−	−			
1d1	+	+	+	+	+	−
1d1′	+	+	+	+	+	−
1d2	+	+	+	+	+	o
1d2′	+	+	+	+	+	+
1d2″	+	+	+	+	+	+
2d1	−	+	+	+	+	o
2d1′	−	o	+	+	+	o
2d2	−	o	+	+	+	o
2d2′	−	+	−			
2d2″	+	+	+	+	+	−
2d4	−	−	−			
1d12	+	+	+	+	−	−
2d12	+	+	+	+	−	−

the case of S_2, Mn^{III}.[132] Assignment is straightforward for these model systems, where the spin projection on the manganese center of larger intrinsic spin is approximately double that of the manganese center of smaller intrinsic spin. However, this is not the case within highly coupled systems such as the OEC. Small intrinsic hyperfine values for Mn^{III} centers have been reported also for mixed valence $Mn^{III}Mn^{IV}$ dimers[133] and have been tentatively attributed to contributions of s character to the spin density at the nucleus of the distorted, five-coordinate center,[134] although further investigation is certainly necessary to fully understand this phenomenon. Therefore, there is an accumulating body of computational data suggesting that the Mn^{III} center does not necessarily have to be assigned the largest hyperfine coupling in such highly connected systems.

3.5. Final OEC Model Evaluation and Implications. In this work, a combined evaluation of structural, energetic, magnetic, and spectroscopic properties was attempted in an effort to determine the structural details of the oxygen evolving complex in the S_2 state. The possible models presented above would otherwise be hard to differentiate based on a single isolated property. For example, the parent models **1** and **2** are effectively isoenergetic even though they have structural differences; however, they are clearly distinguished by their exchange coupling scheme and their ground state spin multiplicity. Similarly, most of the singly deprotonated isomers (series **1d*n*** and **2d*n***) fall within a narrow range of energies and have the same ground spin state but display marked differences in the distribution and magnitude of the ^{55}Mn hyperfine couplings. To provide an accessible overview of the results, a qualitative evaluation of all models with respect to all properties discussed in this paper is given in Table 6. To define reasonable limits, acceptable deviations were considered to be 0.2 Å for metal−metal distances and 5 and 10 kcal mol^{-1} for good and sufficient relative energies, respectively. Only models with ground states of spin 1/2 are considered good. Given the uncertainty involved in the experimental determination of the first energy gap, all models with the correct ground state can be considered adequate. Spin projection patterns of approximately 1.0, −1.0, −1.0, and 2.0 for Mn_A to Mn_D, respectively, were considered good, while the ^{55}Mn hyperfine coupling constants were characterized as good or sufficient if they have rms deviations from the experimental values less than 25 and 35 MHz, respectively. The calculated ^{14}N HFCs are not sufficiently discriminating to be used as an additional criterion (see Supporting Information).

Considering the summary presented in Table 6, and assuming the $Mn_3^{IV}Mn^{III}$ oxidation states of the cluster in the S_2 state, it is expected that the most likely charge in the S_2 state for a model with the composition used in the present work is 0 or +1. Given that the singly deprotonated models, after all the successive stages of evaluation, are favored owing to their hyperfine coupling constants, it appears that the neutral state is preferred. This in turn implies that the S_1 state, which only differs in the number of electrons and not in the number of protons, most probably carries a net negative charge. The doubly deprotonated models, which are negatively charged, are excluded here because of the extremely poor agreement with the experimentally determined ^{55}Mn hyperfine coupling constants. A more negatively charged system would be expected to be unfavorable for efficient proton removal, consistent with the present assignment.

Of importance in establishing correlations to spectroscopy are the differences between models of type **1** and **2** with an OH^- ligand on Mn_A. More specifically, the difference between the effective ground state, $S_t = 1/2$, and the first excited state provides insight into the discrepancy between preparations with and without methanol in higher plants and potentially also into the observed differences between different species.[40] Within our calculations, models of type **1** show a larger energy separation of approximately 25 cm^{-1}, similar to MeOH treated samples. By contrast, models of type **2** with an OH^- ligand on Mn_A have ground state spin 1/2 and smaller first excitation energy gaps, of a few wavenumbers (1−5 cm^{-1}), similar to spinach samples that have not been treated with methanol.[40] It is possible that the behavior observed in the present models reproduces the effect of methanol binding at or close to Mn_A or in the locus formed between Mn_A and Mn_D (water positions 2 and 3) potentially affecting the hydrogen bonding network and even the coordination mode of Glu189. Theoretical and experimental work is currently being done in our laboratories to identify the correct binding site and fully understand the effect of MeOH on the OEC and its electronic structure.

In terms of overall protonation patterns, the present results have important implications for the Kok cycle of the water oxidizing complex. The two most relevant conclusions are the necessary presence of an OH^- ligand on Mn_A and the lack of an OH^- ligand on the Ca^{2+} cofactor. The location of an OH^- ligand on Mn_A in the OEC is shown to be necessary for obtaining appropriate spin projection coefficients. The implications of this hydroxide ligand can be interpreted in the context of the deprotonation events necessary in the Kok cycle for water oxidation; it is our contention that the OH^- ligand facilitates the transfer of

protons out of the active site of the OEC core. The lack of an OH^- located on the Ca^{2+} ion also provides important clues. Here a possible interpretation is that the calcium cofactor holds a structural role in the OEC, whereby the second water molecule used in the cycle is coordinated to Ca^{2+} and thus located in close proximity to the active site. In this sense, we would tentatively identify, in the S_2 state, the fast exchanging substrate water molecule, W_f,[135−137] with the Ca-bound W(3) and the slow exchanging water, Ws, with the μ-oxo bridged O(5) between Mn_A and Mn_B.

The observed preference for a nondeprotonated Ca^{2+}-bound W(3) in the S_2 state hints at the possibility of a nucleophilic water attack of W(3) onto the neighboring oxo bridge between Mn_A and Mn_B or onto a fully deprotonated W(2) during the $S_3 \rightarrow S_4 \rightarrow S_0$ transition. However, this type of mechanism appears energetically unfavorable over oxo/oxyl radical coupling.[50] Additionally, substrate water exchange experiments argue against a terminal Ca-bound substrate water in the S_3 state.[135,136,138] Nevertheless, several variants of the above reaction pathway have been proposed over the years, as well as alternate mechanisms for O_2 evolution, not involving nucleophilic water attack.[10,56,137,139−142] Kusunoki has previously proposed an alternative mechanism involving the formation of O_2 through the terminal W(1) and W(2) ligands on Mn_A.[62,63] It is interesting to note that this mechanism can be considered consistent with the spectroscopic calculations here but suggests that W(2) is a substrate rather than involved in proton transport as suggested above. The work proposed by Siegbahn follows the previously mentioned oxo/oxyl coupling reaction to form O_2. In this case, after deprotonation, a bulk water molecule forms a hydroxide ligand to Mn_D during the $S_2 \rightarrow S_3$ transition.[51] On the basis of the present structural information, we suggest that this ligand on Mn_D would rather be formed by W(3) instead. However, this detail is unlikely to change the low energy barrier O−O bond formation pathway proposed by Siegbahn. The calculations on the S_2 state of the OEC presented here are unfortunately unable to distinguish between these three presented mechanistic alternatives. Indeed, each proposed mechanism can be suitably modified to accommodate the two best models from Table 6 (**1d2′** and **1d2″**).

5. CONCLUSIONS

This work has focused on the S_2 state of the OEC in PSII. An attempt has been made to differentiate between structural models and protonation isomers on the basis of their EPR/ENDOR and EXAFS spectroscopic properties, even when the models were close in energy. The emphasis of the work is the combination of information available from both experiment and theory.

An important result of the present work is the refinement of the recent 1.9 Å X-ray crystal structure of Umena et al.[19] in terms of the bonding within the Mn_4O_5Ca cluster. Upon geometry optimization in the S_2 state, the core relaxes to a less-connected form than that suggested in the crystallographic model, leaving an open coordination site at the Mn^{III} ion. This form is significantly lower in energy, and the loss of the suggested cuboid feature allows the development of antiferromagnetic interactions that permit the system to attain the experimentally consistent low-spin $S = 1/2$ ground state.

From the BS-DFT calculations, it was found that the electronic structure of the OEC is highly sensitive to small changes in the structures. For example, the electronic structure can be significantly tuned by the removal of a proton from a water ligand on Mn_A and/or by a reorientation of Glu189. Changes in the relative orientation of the Glu189 residue, parent models **1** and **2** (see Figure 4), perturb the ground state spin, which can be switched from 1/2 to 7/2 due to a rearrangement of the Jahn−Teller axis on Mn_D. Clearly, the large electronic changes induced from small geometric changes must be reflected in the calculated exchange and hyperfine coupling constants. This, once more, demonstrates that spectroscopic properties might react more sensitively to such changes than the total energy.

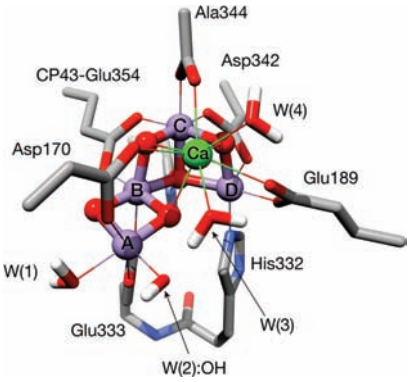

Figure 6. Ⓦ Model **1d2′**, one of the structurally, energetically, and spectroscopically consistent models for the S_2 state of the OEC. An interactive model of the molecule is available as a web-enhanced object in the HTML version.

A comparison of all properties calculated here with experimental data indicates that models **1d2′** and **1d2″** are the most consistent models (Figure 6 and Table 6). Each of these models has a hydroxide ligand on Mn_A similar to the previous work of Siegbahn[47] and the more recent work of Kusunoki.[63] The location of the hydroxide ligand has important implications for the catalytic cycle of the OEC. It is possible that the OH^- ligand facilitates the removal of protons from the substrate water molecules within the Kok cycle. Our results indicate that deprotonation of a Ca^{2+}-bound water is disfavored in the S_2 state of the OEC. Additionally, it appears that further deprotonation of the system is unlikely, as models with two hydroxide ligands on Mn_A have calculated ^{55}Mn hyperfine coupling constants that disagree significantly with experiment. While the agreement with experiment of the **1d2′** and **1d2″** models is good, it should be noted that for the majority of models presented here the maximal isotropic ^{55}Mn HFC is not located on Mn^{III} but on the Mn^{IV} ion, Mn_A. A re-evaluation of EPR/ENDOR data for the OEC in the S_2 state is being pursued in light of this result.

■ ASSOCIATED CONTENT

Ⓢ **Supporting Information.** Details on protocols and procedures for: calculating exchange couplings, energy levels, spin states, and hyperfine coupling constants; structural overlays; absolute energies (in Hartrees) of all optimized structures; intrinsic site hyperfine couplings; ^{14}N hyperfine couplings; and coordinates for selected models. This material is available free of charge via the Internet at http://pubs.acs.org.

Ⓦ **Web Enhanced Feature.** An interactive model of the molecule in Figure 6 is available in the HTML version.

■ AUTHOR INFORMATION

Corresponding Author

johannes.messinger@chem.umu.se; wolfgang.lubitz@mpi-mail.mpg.de; frank.neese@mpi-mail.mpg.de

■ ACKNOWLEDGMENT

We thank the Max Planck Gesellschaft, the University of Bonn, and SOLAR-H2 for financial support of this work. J.M. acknowledges support from the Kempe Stiftelse, the Knut och Alice Wallenberg Foundation, and VR.

■ REFERENCES

(1) *Photosynthesis. Energy from the Sun*; Allen, J. F., Gantt, E., Golbeck, J., Osmond, B., Eds.; Springer: Dordrecht, 2008.
(2) Collings, A. F.; Critchley, C. *Artificial Photosynthesis: From Basic Biology to Industrial Application*; Wiley-VCH: Weinheim, 2005.
(3) Lubitz, W.; Reijerse, E. J.; Messinger, J. *Energy Environ. Sci.* **2008**, *1*, 15.
(4) Lewis, N. S.; Nocera, D. G. *Proc. Natl. Acad. Sci. U.S.A.* **2006**, *103*, 15729.
(5) Blankenship, R. E. *Molecular Mechanisms of Photosynthesis*; Blackwell: Oxford, 2001.
(6) Joliot, P.; Barbieri, G.; Chabaud, R. *Photochem. Photobiol.* **1969**, *10*, 309.
(7) Kok, B.; Forbush, B.; McGloin, M. *Photochem. Photobiol.* **1970**, *11*, 457.
(8) Suzuki, H.; Sugiura, M.; Noguchi, T. *J. Am. Chem. Soc.* **2009**, *131*, 7849.
(9) Dau, H.; Haumann, M. *Coord. Chem. Rev.* **2008**, *252*, 273.
(10) Dau, H.; Haumann, M. *Biochim. Biophys. Acta Bioenerg.* **2007**, *1767*, 472.
(11) Pushkar, Y.; Yano, J.; Sauer, K.; Boussac, A.; Yachandra, V. K. *Proc. Natl. Acad. Sci.* **2008**, *105*, 1879.
(12) Zouni, A.; Witt, H. T.; Kern, J.; Fromme, P.; Krauss, N.; Saenger, W.; Orth, P. *Nature* **2001**, *409*, 739.
(13) Kamiya, N.; Shen, J.-R. *Proc. Natl. Acad. Sci. U.S.A.* **2003**, *100*, 98.
(14) Ferreira, K. N.; Iverson, T. M.; Maghlaoui, K.; Barber, J.; Iwata, S. *Science* **2004**, *303*, 1831.
(15) Biesiadka, J.; Loll, B.; Kern, J.; Irrgang, K.-D.; Zouni, A. *Phys. Chem. Chem. Phys.* **2004**, *6*, 4733.
(16) Loll, B.; Kern, J.; Saenger, W.; Zouni, A.; Biesiadka, J. *Nature* **2005**, *438*, 1040.
(17) Guskov, A.; Kern, J.; Gabdulkhakov, A.; Broser, M.; Zouni, A.; Saenger, W. *Nat. Struct. Mol. Biol.* **2009**, *16*, 334.
(18) Guskov, A.; Gabdulkhakov, A.; Broser, M.; Glockner, C.; Hellmich, J.; Kern, J.; Frank, J.; Muh, F.; Saenger, W.; Zouni, A. *ChemPhysChem* **2010**, *11*, 1160.
(19) Umena, Y.; Kawakami, K.; Shen, J.-R.; Kamiya, N. *Nature* **2011**, *473*, 55.
(20) Murray, J. W.; Maghlaoui, K.; Kargul, J.; Ishida, N.; Lai, T.-L.; Rutherford, A. W.; Sugiura, M.; Boussac, A.; Barber, J. *Energy Environ. Sci.* **2008**, *1*, 161.
(21) Kawakami, K.; Umena, Y.; Kamiya, N.; Shen, J.-R. *Proc. Natl. Acad. Sci.* **2009**, *106*, 8567.
(22) Yocum, C. F. *Coord. Chem. Rev.* **2008**, *252*, 296.
(23) Yano, J.; Kern, J.; Irrgang, K.-D.; Latimer, M. J.; Bergmann, U.; Glatzel, P.; Pushkar, Y.; Biesiadka, J.; Loll, B.; Sauer, K.; Messinger, J.; Zouni, A.; Yachandra, V. K. *Proc. Natl. Acad. Sci. U.S.A.* **2005**, *102*, 12047.
(24) Robblee, J. H.; Messinger, J.; Cinco, R. M.; McFarlane, K. L.; Fernandez, C.; Pizarro, S. A.; Sauer, K.; Yachandra, V. K. *J. Am. Chem. Soc.* **2002**, *124*, 7459.
(25) Cinco, R. M.; Robblee, J. H.; Messinger, J.; Fernandez, C.; Holman, K. L. M.; Sauer, K.; Yachandra, V. K. *Biochemistry* **2004**, *43*, 13271.
(26) Yano, J.; Pushkar, Y.; Glatzel, P.; Lewis, A.; Sauer, K.; Messinger, J.; Bergmann, U.; Yachandra, V. *J. Am. Chem. Soc.* **2005**, *127*, 14974.
(27) Yano, J.; Kern, J.; Sauer, K.; Latimer, M. J.; Pushkar, Y.; Biesiadka, J.; Loll, B.; Saenger, W.; Messinger, J.; Zouni, A.; Yachandra, V. K. *Science* **2006**, *314*, 821.
(28) Pushkar, Y.; Yano, J.; Glatzel, P.; Messinger, J.; Lewis, A.; Sauer, K.; Bergmann, U.; Yachandra, V. *J. Biol. Chem.* **2007**, *282*, 7198.
(29) Yano, J.; Yachandra, V. *Photosynth. Res.* **2007**, *92*, 289.
(30) Sauer, K.; Yano, J.; Yachandra, V. K. *Photosynth. Res.* **2005**, *85*, 73.
(31) Sauer, K.; Yano, J.; Yachandra, V. K. *Coord. Chem. Rev.* **2008**, *252*, 318.
(32) Yano, J.; Yachandra, V. K. *Inorg. Chem.* **2008**, *47*, 1711.
(33) Kulik, L. V.; Epel, B.; Lubitz, W.; Messinger, J. *J. Am. Chem. Soc.* **2005**, *127*, 2392.
(34) Kulik, L. V.; Epel, B.; Lubitz, W.; Messinger, J. *J. Am. Chem. Soc.* **2007**, *129*, 13421.
(35) Teutloff, C.; Keflen, S.; Kern, J.; Zouni, A.; Bittl, R. *FEBS Lett.* **2006**, *580*, 3605.
(36) Teutloff, C.; Pudollek, S.; Keßen, S.; Broser, M.; Zouni, A.; Bittl, R. *Phys. Chem. Chem. Phys.* **2009**, *11*, 6715.
(37) Peloquin, J. M.; Campbell, K. A.; Randall, D. W.; Evanchik, M. A.; Pecoraro, V. L.; Armstrong, W. H.; Britt, R. D. *J. Am. Chem. Soc.* **2000**, *122*, 10926.
(38) Charlot, M.-F.; Boussac, A.; Blondin, G. *Biochim. Biophys. Acta* **2005**, *1708*, 120.
(39) Pudollek, S.; Lendzian, F.; Bittl, R. *Biochem. Soc. Trans.* **2008**, *36*, 1001.
(40) Su, J.-H.; Cox, N.; Ames, W.; Pantazis, D. A.; Rapatskiy, L.; Lohmiller, T.; Kulik, L. V.; Dorlet, P.; Rutherford, A. W.; Neese, F.; Boussac, A.; Lubitz, W.; Messinger, J. *Biochim. Biophys. Acta Bioenerg.* **2011**, *1807*, 829.
(41) Cox, N.; Rapatskiy, L.; Su, J.-H.; Pantazis, D. A.; Sugiura, M.; Kulik, L.; Dorlet, P.; Rutherford, A. W.; Neese, F.; Boussac, A.; Lubitz, W.; Messinger, J. *J. Am. Chem. Soc.* **2011**, *133*, 3635.
(42) Dismukes, G. C.; Siderer, Y. *Proc. Natl. Acad. Sci. U.S.A.* **1981**, *78*, 274.
(43) Hansson, O.; Andreasson, L. E. *Biochim. Biophys. Acta* **1982**, *679*, 261.
(44) Buda, F. *Photosynth. Res.* **2009**, *102*, 437.
(45) Orio, M.; Pantazis, D. A.; Neese, F. *Photosynth. Res.* **2009**, *102*, 443.
(46) Sproviero, E.; Newcomer, M.; Gascón, J.; Batista, E.; Brudvig, G.; Batista, V. *Photosynth. Res.* **2009**, *102*, 455.
(47) Siegbahn, P. E. M. *Acc. Chem. Res.* **2009**, *42*, 1871.
(48) Lundberg, M.; Siegbahn, P. E. M. *Phys. Chem. Chem. Phys.* **2004**, *6*, 4772.
(49) Siegbahn, P. E. M.; Blomberg, M. R. A. *Philos. Trans. R. Soc. London, Ser. A* **2005**, *363*, 847.
(50) Siegbahn, P. E. M. *Chem.—Eur. J.* **2006**, *12*, 9217.
(51) Siegbahn, P. E. M. *Chem.—Eur. J.* **2008**, *14*, 8290.
(52) Siegbahn, P. E. M. *Inorg. Chem.* **2008**, *47*, 1779.
(53) Schinzel, S.; Schraut, J.; Arbuznikov, A.; Siegbahn, P.; Kaupp, M. *Chem.—Eur. J.* **2010**, *16*, 10424.
(54) Sproviero, E. M.; Gascon, J. A.; McEvoy, J. P.; Brudvig, G. W.; Batista, V. S. *J. Chem. Theory Comput.* **2006**, *2*, 1119.
(55) Sproviero, E. M.; Gascon, J. A.; McEvoy, J. P.; Brudvig, G. W.; Batista, V. S. *J. Am. Chem. Soc.* **2008**, *130*, 6728.
(56) Sproviero, E. M.; Gascon, J. A.; McEvoy, J. P.; Brudvig, G. W.; Batista, V. S. *J. Am. Chem. Soc.* **2008**, *130*, 3428.
(57) Sproviero, E. M.; Shinopoulos, K.; Gascon, J. A.; McEvoy, J. P.; Brudvig, G. W.; Batista, V. S. *Phil. Trans. R. Soc. B* **2008**, *363*, 1149.
(58) Sproviero, E. M.; Gascon, J. A.; McEvoy, J. P.; Brudvig, G. W.; Batista, V. S. *Coord. Chem. Rev.* **2008**, *252*, 395.
(59) Petrie, S.; Stranger, R.; Gatt, P.; Pace, R. J. *Chem.—Eur. J.* **2007**, *13*, 5082.
(60) Petrie, S.; Stranger, R.; Pace, R. L. *Chem.—Eur. J.* **2008**, *14*, 5482.
(61) Isobe, H.; Shoji, M.; Koizumi, K.; Kitagawa, Y.; Yamanaka, S.; Kuramitsu, S.; Yamaguchi, K. *Polyhedron* **2005**, *24*, 2767.
(62) Kusunoki, M. *Biochim. Biophys. Acta Bioenerg.* **2007**, *1767*, 484.
(63) Kusunoki, M. *Photochem. Photobiol. B* **2011**, *104*, 100.

(64) Yamaguchi, K.; Yamanaka, S.; Isobe, H.; Shoji, M.; Koizumi, K.; Kitagawa, Y.; Kawakami, T.; Okumura, M. *Polyhedron* **2007**, *26*, 2216.
(65) Zein, S.; Kulik, L. V.; Yano, J.; Kern, J.; Pushkar, Y.; Zouni, A.; Yachandra, V. K.; Lubitz, W.; Neese, F.; Messinger, J. *Phil. Trans. R. Soc. B* **2008**, *363*, 1167.
(66) Pantazis, D. A.; Orio, M.; Petrenko, T.; Zein, S.; Bill, E.; Lubitz, W.; Messinger, J.; Neese, F. *Chem.—Eur. J.* **2009**, *15*, 5108.
(67) Pantazis, D. A.; Orio, M.; Petrenko, T.; Zein, S.; Lubitz, W.; Messinger, J.; Neese, F. *Phys. Chem. Chem. Phys.* **2009**, *11*, 6788.
(68) Orio, M.; Pantazis, D. A.; Petrenko, T.; Neese, F. *Inorg. Chem.* **2009**, *48*, 7251.
(69) Sinnecker, S.; Neese, F.; Noodleman, L.; Lubitz, W. *J. Am. Chem. Soc.* **2004**, *126*, 2613.
(70) Pantazis, D. A.; Krewald, V.; Orio, M.; Neese, F. *J. Chem. Soc., Dalton Trans.* **2010**, *39*, 4959.
(71) Lassalle-Kaiser, B.; Hureau, C.; Pantazis, D. A.; Pushkar, Y.; Guillot, R.; Yachandra, V. K.; Yano, J.; Neese, F.; Anxolabehere-Mallart, E. *Energy Environ. Sci.* **2010**, *3*, 924.
(72) Baffert, C.; Orio, M.; Pantazis, D. A.; Duboc, C.; Blackman, A. G.; Blondin, G.; Neese, F.; Deronzier, A.; Collomb, M.-N. *Inorg. Chem.* **2009**, *48*, 10281.
(73) Becke, A. D. *Phys. Rev. A* **1988**, *38*, 3098.
(74) Perdew, J. P. *Phys. Rev. B* **1986**, *33*, 8822.
(75) Neese, F. *J. Biol. Inorg. Chem.* **2006**, *11*, 702.
(76) Neese, F. *Coord. Chem. Rev.* **2009**, *253*, 526.
(77) Neese, F.; Ames, W.; Christian, G.; Kampa, M.; Liakos, D. G.; Pantazis, D. A.; Roemelt, M.; Surawatanawong, P.; Ye, S. F. *Adv. Inorg. Chem.* **2010**, *62*, 301.
(78) Grimme, S. *J. Comput. Chem.* **2004**, *25*, 1463.
(79) Grimme, S. *J. Comput. Chem.* **2006**, *27*, 1787.
(80) Grimme, S.; Antony, J.; Schwabe, T.; Muck-Lichtenfeld, C. *Org. Biomol. Chem.* **2007**, *5*, 741.
(81) Siegbahn, P. E. M.; Blomberg, M. R. A.; Chen, S.-L. *J. Chem. Theory Comput.* **2010**, *6*, 2040.
(82) Grimme, S.; Antony, J.; Ehrlich, S.; Krieg, H. *J. Chem. Phys.* **2010**, *132*, 154104.
(83) van Lenthe, E.; Baerends, E. J.; Snijders, J. G. *J. Chem. Phys.* **1993**, *99*, 4597.
(84) van Lenthe, E.; Baerends, E. J.; Snijders, J. G. *J. Chem. Phys.* **1994**, *101*, 9783.
(85) van Wüllen, C. *J. Chem. Phys.* **1998**, *109*, 392.
(86) Pantazis, D. A.; Chen, X. Y.; Landis, C. R.; Neese, F. *J. Chem. Theory Comput.* **2008**, *4*, 908.
(87) Weigend, F.; Ahlrichs, R. *Phys. Chem. Chem. Phys.* **2005**, *7*, 3297.
(88) Klamt, A.; Schüürman, D. *J. Chem. Soc., Perkin Trans. 2* **1993**, 799.
(89) Sinnecker, S.; Rajendran, A.; Klamt, A.; Diedenhofen, M.; Neese, F. *J. Phys. Chem. A* **2006**, *110*, 2235.
(90) Weigend, F. *Phys. Chem. Chem. Phys.* **2006**, *8*, 1057.
(91) Neese, F.; *ORCA — an ab initio, Density Functional and Semiempirical Program Package (v. 2.8.0)*; Universität Bonn: Bonn, Germany, 2010.
(92) Noodleman, L. *J. Chem. Phys.* **1981**, *74*, 5737.
(93) Noodleman, L.; Davidson, E. R. *Chem. Phys.* **1986**, *109*, 131.
(94) Noodleman, L.; Case, D. A. *Adv. Inorg. Chem.* **1992**, *38*, 423.
(95) Staroverov, V. N.; Scuseria, G. E.; Tao, J.; Perdew, J. P. *J. Chem. Phys.* **2003**, *119*, 12129.
(96) Neese, F.; Wennmohs, F.; Hansen, A.; Becker, U. *Chem. Phys.* **2009**, *356*, 98.
(97) Neese, F. *J. Chem. Phys.* **2003**, *118*, 3939.
(98) Munzarová, M.; Kaupp, M. *J. Phys. Chem. A* **1999**, *103*, 9966.
(99) Malkin, E.; Malkin, I.; Malkina, O. L.; Malkin, V. G.; Kaupp, M. *Phys. Chem. Chem. Phys.* **2006**, *8*, 4079.
(100) Kabsch, W. *Acta Crystallogr., Sect. A* **1976**, *32*, 922.
(101) Eargle, J.; Wright, D.; Luthey-Schulten, Z. *Bioinformatics* **2006**, *22*, 504.
(102) Shindyalov, I. N.; Bourne, P. E. *Protein Eng.* **1998**, *11*, 739.
(103) Debus, R. J. *Coord. Chem. Rev.* **2008**, *252*, 244.
(104) Horner, O.; Anxolabéhère-Mallart, E.; Charlot, M. F.; Tchertanov, L.; Guilhem, J.; Mattioli, T. A.; Boussac, A.; Girerd, J. J. *Inorg. Chem.* **1999**, *38*, 1222.
(105) Jensen, A. F.; Su, Z.; Hansen, N. K.; Larsen, F. K. *Inorg. Chem.* **1995**, *34*, 4244.
(106) Hureau, C.; Blondin, G.; Cesario, M.; Un, S. *J. Am. Chem. Soc.* **2003**, *125*, 11637.
(107) Frapart, Y. M.; Boussac, A.; Albach, R.; Anxolabéhère-Mallart, E.; Delroisse, M.; Verlhac, J. B.; Blondin, G.; Girerd, J. J.; Guilhem, J.; Cesario, M.; Rutherford, A. W.; Lexa, D. *J. Am. Chem. Soc.* **1996**, *118*, 2669.
(108) Horner, O.; Charlot, M. F.; Boussac, A.; Anxolabéhère-Mallart, E.; Tchertanov, L.; Guilhem, J.; Girerd, J. J. *Eur. J. Inorg. Chem.* **1998**, *1998*, 721.
(109) Goodson, P. A.; Glerup, J.; Hodgson, D. J.; Michelsen, K.; Pedersen, E. *Inorg. Chem.* **1990**, *29*, 503.
(110) Hagen, K. S.; Armstrong, W. H.; Hope, H. *Inorg. Chem.* **1988**, *27*, 967.
(111) Suzuki, M.; Senda, H.; Kobayashi, Y.; Oshio, H.; Uehara, A. *Chem. Lett.* **1988**, *17*, 1763.
(112) Wieghardt, K.; Bossek, U.; Zsolnai, L.; Huttner, G.; Blondin, G.; Girerd, J. J.; Babonneau, F. *J. Chem. Soc., Chem. Commun.* **1987**, 651.
(113) Pal, S.; Gohdes, J. W.; Wilisch, W. C. A.; Armstrong, W. H. *Inorg. Chem.* **1992**, *31*, 713.
(114) Pal, S.; Olmstead, M. M.; Armstrong, W. H. *Inorg. Chem.* **1995**, *34*, 4708.
(115) Grundmeier, A.; Dau, H. *Biochim. Biophys. Acta* **2011**, doi: 10.1016/j.bbabio.2011.07.004.
(116) Wydrzynski, T.; Hillier, W.; Messinger, J. *Physiol. Plant.* **1996**, *96*, 342.
(117) Messinger, J.; Wacker, U.; Renger, G. *Biochemistry* **1991**, *30*, 7852.
(118) Aznar, C. P.; Britt, R. D. *Phil. Trans. R. Soc. B* **2002**, *357*, 1359.
(119) Yachandra, V. K.; Sauer, K.; Klein, M. P. *Chem. Rev.* **1996**, *96*, 2927.
(120) Carrell, T. G.; Tyryshkin, A. M.; Dismukes, G. C. *J. Biol. Inorg. Chem.* **2002**, *7*, 2.
(121) Luber, S.; Rivalta, I.; Umena, Y.; Kawakami, K.; Shen, J.-R.; Kamiya, N.; Brudvig, G. W.; Batista, V. S. *Biochemistry* **2011**, *50*, 6308.
(122) Dau, H.; Grundmeier, A.; Loja, P.; Haumann, M. *Phil. Trans. R. Soc. B* **2008**, *363*, 1237.
(123) Siegbahn, P. E. M. *J. Am. Chem. Soc.* **2009**, *131*, 18238.
(124) Renger, G. *J. Photochem. Photobiol. B: Biol.* **2011**, *104*, 35.
(125) Renger, G. *Biochim. Biophys. Acta Bioenerg.* **2001**, *1503*, 210.
(126) Schäfer, K. O.; Bittl, R.; Zweygart, W.; Lendzian, F.; Haselhorst, G.; Weyhermüller, T.; Wieghardt, K.; Lubitz, W. *J. Am. Chem. Soc.* **1998**, *120*, 13104.
(127) Zheng, M.; Khangulov, S. V.; Dismukes, G. C.; Barynin, V. V. *Inorg. Chem.* **1994**, *33*, 382.
(128) Randall, D. W.; Sturgeon, B. E.; Ball, J. A.; Lorigan, G. A.; Chan, M. K.; Klein, M. P.; Armstrong, W. H.; Britt, R. D. *J. Am. Chem. Soc.* **1995**, *117*, 11780.
(129) Yeagle, G. J.; Gilchrist, M. L.; McCarrick, R. M.; Britt, R. D. *Inorg. Chem.* **2008**, *47*, 1803.
(130) Petrie, S.; Stranger, R.; Pace, R. J. *Angew. Chem., Int. Ed.* **2010**, *49*, 4233.
(131) Petrie, S.; Stranger, R.; Pace, R. J. *Chem.—Eur. J* **2010**, *16*, 14026.
(132) Teutloff, C.; Schafer, K. O.; Sinnecker, S.; Barynin, V.; Bittl, R.; Wieghardt, K.; Lendzian, F.; Lubitz, W. *Magn. Reson. Chem.* **2005**, *43*, S51.
(133) Schinzel, S.; Kaupp, M. *Can. J. Chem.* **2009**, *87*, 1521.
(134) Munzarová, M. L.; Kubáček, P.; Kaupp, M. *J. Am. Chem. Soc.* **2000**, *122*, 11900.
(135) Messinger, J.; Badger, M.; Wydrzynski, T. *Proc. Natl. Acad. Sci. U.S.A.* **1995**, *92*, 3209.

(136) Hillier, W.; Messinger, J.; Wydrzynski, T. *Biochemistry* **1998**, *37*, 16908.
(137) Messinger, J. *Phys. Chem. Chem. Phys.* **2004**, *6*, 4764.
(138) Hendry, G.; Wydrzynski, T. *Biochemistry* **2003**, *42*, 6209.
(139) McEvoy, J. P.; Brudvig, G. W. *Chem. Rev.* **2006**, *106*, 4455.
(140) Hillier, W.; Messinger, J. In *Photosystem II*; Wydrzynski, T., Satoh, K., Freeman, J., Eds.; Springer: Netherlands, 2005; Vol. 22, p 567.
(141) Messinger, J.; Renger, G. In *Primary Processes of Photosynthesis, Part 2: Principles and Apparatus*; The Royal Society of Chemistry: 2008; Vol. 9, p 291.
(142) Dau, H.; Limberg, C.; Reier, T.; Risch, M.; Roggan, S.; Strasser, P. *ChemCatChem* **2010**, *2*, 724.